THE JOURNAL OF BIOLOGICAL CHEMISTRY VOL. 288, NO. 49, pp. 35014–35027, December 6, 2013

Binding of G-quadruplexes to the N-terminal Recognition Domain of the RNA Helicase Associated with AU-rich Element (RHAU)*

Received for publication, August 23, 2013, and in revised form, October 16, 2013 Published, JBC Papers in Press, October 22, 2013, DOI 10.1074/jbc.M113.512970

Markus Meier[‡1], Trushar R. Patel[‡1,2], Evan P. Booy[‡3], Oksana Marushchak[‡], Natalie Okun[‡4], Soumya Deo[‡5], Ryan Howard[‡6], Kevin McEleney[§], Stephen E. Harding[¶], Jörg Stetefeld[‡‖7], and Sean A. McKenna[‡‖8]

From the Departments of [‡]Chemistry and [‖]Biochemistry and Medical Genetics and [§]Manitoba Institute for Materials, University of Manitoba, Winnipeg, Manitoba R3T 2N2, Canada and [¶]National Centre for Macromolecular Hydrodynamics Laboratory, School of Biosciences, University of Nottingham, Sutton Bonington LE12 5RD, United Kingdom

Background: The helicase RHAU requires an N-terminal extension to bind quadruplex structures.
Results: This extension adopts an elongated shape and interacts with the guanine tetrad face of quadruplexes.
Conclusion: We provide a basis for the understanding of quadruplex binding by the N-terminal domain.
Significance: The N-terminal region does not require the 2′-OH of the ribose to mediate the protein-quadruplex interaction.

Polynucleotides containing consecutive tracts of guanines can adopt an intramolecular G-quadruplex structure where multiple planar tetrads of hydrogen-bound guanines stack on top of each other. Remodeling of G-quadruplexes impacts numerous aspects of nucleotide biology including transcriptional and translational control. RNA helicase associated with AU-rich element (RHAU), a member of the ATP-dependent DEX(H/D) family of RNA helicases, has been established as a major cellular quadruplex resolvase. RHAU contains a core helicase domain responsible for ATP binding/hydrolysis/helicase activity and is flanked on either side by N- and C-terminal extensions. The N-terminal extension is required for quadruplex recognition, and we have previously demonstrated complex formation between this domain and a quadruplex from human telomerase RNA. Here we used an integrated approach that includes small angle x-ray scattering, nuclear magnetic resonance spectroscopy, circular dichroism, and dynamic light scattering methods to demonstrate the recognition of G-quadruplexes by the N-terminal domain of RHAU. Based on our results, we conclude that (i) quadruplex from the human telomerase RNA and its DNA analog both adopt a disc shape in solution, (ii) $RHAU_{53-105}$ adopts a defined and extended conformation in solution, and (iii) the N-terminal domain mediates an interaction with a guanine tetrad face of quadruplexes. Together, these data form the foundation for understanding the recognition of quadruplexes by the N-terminal domain of RHAU.

G-quadruplex structures spontaneously fold from RNA or DNA sequences containing consecutive runs of two or more adjacent guanines (G-tracts) and assemble into stable stacks of planar G-quartets that are stabilized by π-stacking interactions (1–7). Quadruplexes are further stabilized by monovalent cations (typically K^+ or Na^+) that interact with guanine O6 oxygens at the center of the quadruplex (8). A diversity of quadruplex structures can assemble as either parallel or antiparallel configurations that vary based on the composition and length of intervening loops between guanines within a G-tract or between tracts themselves (9). Although the formation of quadruplexes in compatible sequences of DNA and RNA was originally considered to be an *in vitro* artifact of laboratory research, there is now compelling evidence that suggests that their formation *in vivo* may have great importance to a variety of biochemical processes (10, 11). *In silico* studies suggest a widespread prevalence of RNA and DNA quadruplexes, and this trend has been confirmed experimentally by several studies that demonstrate that formation of G-quadruplexes impacts transcriptional control in promoter regions of genes and modulates translational repression or activation via quadruplex formation in the untranslated regions (UTRs) of mRNAs (12–16). Given that melting temperatures of quadruplexes are much higher than physiological temperature, manipulation of these unusually stable structures to provide regulatory control requires the work of specialized enzymes in living systems.

RNA helicase associated with AU-rich element (RHAU[9]; also known as DHX36 and G4R1) has been recognized as a major

* This work was supported in part by Canadian Institutes of Health Research (CIHR)/Manitoba Health Research Council (MHRC) Regional Partnership Program Grant RPA-118069.
[1] Both authors contributed equally to the data collection, analysis, and manuscript preparation.
[2] Supported by a CIHR postdoctoral fellowship.
[3] Supported by an MHRC postdoctoral fellowship.
[4] Supported by a University of Manitoba Faculty of Science undergraduate student research award and a University of Manitoba undergraduate research fellowship.
[5] Supported by a University of Manitoba graduate fellowship.
[6] Supported by a University of Manitoba undergraduate research fellowship.
[7] Supported by the Canada Research Chair program. To whom correspondence may be addressed: Dept. of Chemistry, University of Manitoba, 144 Dysart Rd., Winnipeg, Manitoba R3T 2N2, Canada. Tel.: 204-474-9731; Fax: 204-474-7608; E-mail: Jorg.Stetefeld@umanitoba.ca.
[8] To whom correspondence may be addressed: Dept. of Chemistry, University of Manitoba, 144 Dysart Rd., Winnipeg, Manitoba R3T 2N2, Canada. Tel.: 204-272-1562; Fax: 204-474-7608; E-mail: Sean.McKenna@umanitoba.ca.

[9] The abbreviations used are: RHAU, RNA helicase associated with AU-rich element; DLS, dynamic light scattering; HSQC, heteronuclear single quantum coherence; D_{max}, maximum particle dimension; hTR, human telomerase RNA; NSD, normalized spatial discrepancy; $P(r)$, pair distance distribution function; R_g, radius of gyration; R_h, hydrodynamic radius; RSM, RHAU-specific motif; $s^0_{20,w}$, sedimentation coefficient corrected to standard conditions (water at 20 °C); SAXS, small angle x-ray scattering; SEC, size exclusion chromatography; HSQC, heteronuclear single quantum correlation.

source of quadruplex-resolving activity in cell lysates (17, 18). RHAU belongs to the DE*X*(H/D) family of RNA helicases, a large group of enzymes that remodel nucleic acid structures in an ATP-dependent manner (19). Recently, specific functional roles for RHAU have emerged. Microarray studies have implicated RHAU in broad spectrum transcriptional regulation and mRNA stability (20). In support, RHAU has been shown to control gene expression through direct binding to quadruplexes within the promoter of the *YY1* gene (21). RHAU can also modulate quadruplex structures in the context of non-coding RNAs. We have previously demonstrated that RHAU associates with a G-quadruplex at the 5′-end of human telomerase RNA (hTR) and is capable of unwinding this quadruplex *in vitro* (22). Interestingly, RHAU can associate with hTR in the context of the telomerase holoenzyme, an interaction that correlates with telomerase activity (23, 24). G-tract substitutions in the quadruplex-forming region of hTR appear to confirm these results (23–25). Taken together, recognition and remodeling of quadruplex structures by RHAU play a central role in a number of key cellular regulatory processes.

RHAU is highly specific for G-quadruplex structures over duplex and single-stranded regions, and although RHAU has been shown to have affinity for both RNA and DNA, enhanced affinity for RNA structures has been reported (17). RHAU contains a core helicase domain (~470 amino acids) responsible for ATP binding/hydrolysis/helicase activity and is flanked on either side by N- and C-terminal extensions (26). The C-terminal extension contains a predicted companion domain to the helicase domain based on sequence homology (residues 682–920), although its biological role is unknown (27). Preceded by a Gly-rich region (residues 10–51), the N-terminal domain extends into a RHAU-specific motif (RSM; residues 54–66), which has been demonstrated to be required for interaction with a synthetic tetramolecular RNA quadruplex (26, 28). The RSM dependence is highlighted by the fact that it is the only conserved element within the N-terminal extension in the *Drosophila* RHAU ortholog (26). Deletion of the RSM attenuates quadruplex binding and unwinding, and a similar effect is observed upon mutagenesis of conserved small (Gly-59 and Gly-63) and hydrophobic (Leu-57 and Ile-62) residues in the RSM (26). Interestingly, mutation of basic RSM residues (Lys-58 and Arg-60) has no negative effect on quadruplex binding.

Although the importance of G-quadruplexes to a myriad of cellular processes is an emerging theme, there is scant information regarding the recognition of this structural motif by proteins. Here we present a comprehensive study detailing the interaction between the N-terminal domain of RHAU and an established binding partner, a G-quadruplex from the 5′-end of the human telomerase RNA. We specifically focused on an N-terminal RHAU construct containing the RSM and demonstrate that it adopts an extended conformation capable of mediating an interaction with both RNA and DNA quadruplexes. Based on our experimental approach, we propose a model in which the RSM recognizes the guanine tetrad face.

EXPERIMENTAL PROCEDURES

Quadruplex Production and Purification—Synthetic hTR_{1-20} RNA (5′-GGGUUGCGGAGGGUGGGCCU-3′, where the underlining highlights the guanines; Integrated DNA Technologies) was dissolved in 20 mM HEPES, pH 7.5, 100 mM KCl, 1 mM EDTA at a concentration of 5 μM. RNA was heated to 95 °C for 5 min, allowed to passively cool to room temperature outside the heat bath, and then purified by SEC on a HiLoad Superdex™ 75 26/60 size exclusion chromatography column ($ÄKTA_{FPLC}$, GE Healthcare). Synthetic DNA quadruplexes (Alpha DNA, Canada) were dissolved in the above HEPES buffer but without adding EDTA, heated to 95 °C, and allowed to cool slowly to room temperature inside the metal heat block or water bath. In contrast to hTR_{1-20}, the DNA_{1-20} elutes as two partially overlapping but distinct quadruplex-containing peaks from the HiLoad Superdex 75 26/60 SEC column. We termed the first peak to elute as $DNA_{1-20}{}^{C1}$ and the second peak as $DNA_{1-20}{}^{C2}$. Whereas purified $DNA_{1-20}{}^{C1}$ can be converted into a mixture of $DNA_{1-20}{}^{C1}$ and $DNA_{1-20}{}^{C2}$ by the heating and cooling procedure described above, $DNA_{1-20}{}^{C2}$ reverts only to the $DNA_{1-20}{}^{C2}$ form. Purified conformations are stable at 4 °C and show no tendency to interconvert during the 4-month period we monitored. All DNA synthesis batches exhibited the same result. Extinction coefficients ($\epsilon_{260\,nm}$) were calculated from the sequence using IDT SciTools® (PrimerQuest® program, Integrated DNA Technologies) and corrected for hyperchromicity using the absorption spectra at 20 and 80 °C: hTR_{1-20}, 173,467 ± 50 M^{-1} cm^{-1}; $DNA_{1-20}{}^{C1}$, 182,040 ± 197 M^{-1} cm^{-1}; $DNA_{1-20}{}^{C2}$, 191,654 ± 157 M^{-1} cm^{-1}. For comparison, established G4 RNA (hTR_{1-43}, GGGUUGCGGAGGGUGGGCCUGGGAGGGGUGGUGGCCAUUUUUU) (22) and dsRNA (HIV-1 trans-activation response element, GGUCUCUCUGGUUAAGCCAGAUCUGAGCCUGGGAGCUCUCUGGCUAACUAGGGAACC) (29) controls were used.

Protein Expression and Purification—$RHAU_{53-105}$ was cloned, expressed, and purified as described previously (22) with a final polishing step of size exclusion chromatography on a Superdex 200 10/300 GL column (GE Healthcare) in 10 mM HEPES, pH 7.5, 150 mM sodium chloride (I = 154 mM) after removal of the hexahistidine (His_6) tag by thrombin. Protein identity was confirmed by mass spectrometry. $RHAU_{53-209}$ was initially cloned, expressed, and purified in an identical manner, but upon analysis by both gel electrophoresis and mass spectrometry, it was determined that a stable proteolytic product corresponding to $RHAU_{53-150}$ had been produced. Isotopically enriched ^{15}N- and ^{15}N,^{13}C-labeled $RHAU_{53-105}$ (or $RHAU_{53-150}$) was overexpressed in M9 minimal medium as described previously (30). The concentration of $RHAU_{53-105}$ and $RHAU_{53-150}$ was measured spectrophotometrically at 280 nm using extinction coefficients of 7020 and 13,980 M^{-1} cm^{-1}, respectively, that were calculated from the sequence using the ExPASy ProtParam tool (31).

Protein·Quadruplex Complex Assembly—Protein and quadruplexes were prepared separately as described above; diluted to 10 μM in 20 mM HEPES, pH 7.5, 100 mM KCl; mixed in an equimolar ratio; gently shaken for 15 min on a rotator; and then concentrated to a convenient volume. Afterward, the complexes were purified on a Superdex 200 10/300 GL SEC column. Complex concentration was determined by UV absorption

using the extinction coefficient ($\epsilon_{260\ nm}$) of the nucleic acid component.

RHAU Association with RNA Quadruplex—All siRNA knockdowns, Western blotting, electrophoretic mobility shift assays, and RNA co-immunoprecipitations in HEK293T cells were performed as described previously (22) with the exception of the His_6-$RHAU_{53-105}$ immunoprecipitations in which 1 mg of cell lysate was supplemented with 350 nM His_6-$RHAU_{53-105}$ for 30 min followed by immunoprecipitation with 10 μg of anti-His_6 antibody (Abcam) for 30 min with end-over-end mixing.

Hydrodynamic Characterization—Sedimentation velocity data of $RHAU_{53-105}$ were collected at 45,000 rpm (20 °C) at 10-min intervals as described previously (32). Sedimentation coefficient values ($s_{20,b}$) obtained at multiple concentrations were corrected to the standard solvent conditions to obtain $s_{20,w}$ values, which were then plotted against concentration to obtain the $s^0_{20,w}$. DLS data were collected as reported previously (33). All samples were subjected to filtration through a 0.1-μm filter (Millipore) and equilibrated for 5 min at 20 °C prior to the measurements. The sedimentation coefficient and hydrodynamic radius (R_h) information from analytical ultracentrifugation and DLS, respectively, were combined using a modified Svedberg equation and yielded a molecular mass of 6.7 kDa for $RHAU_{53-105}$.

UV-Visible Absorption Spectroscopy—UV-visible spectra were recorded on an Evolution 260 Bio spectrophotometer (Thermo Scientific) using a temperature-controlled 1.0-mm sample cell and a 1.0-mm water-filled reference cell. Samples and buffer were measured at each temperature in triplicate. The averaged buffer spectra were subtracted from the corresponding averaged sample spectra.

Spectropolarimetry—All spectra were recorded on a calibrated (2.583 mM (1*S*)-(+)-camphor-10-sulfonic acid monohydrate; Alfa Aesar) J-810 spectropolarimeter (Jasco Inc.). From 350 to 220 nm, a 1.0-mm cell was used with an integration time of 8 s; from 220 to 200 nm, a 1.0-mm cell and 32-s integration time were used; and from 220 to 180 nm, a 0.1-mm cell and an integration time of 32 s were used. We used sample concentrations of 30–50 μM in the 1.0-mm cell and 200 μM in the 0.1-mm cell. In all cases, sample and buffer were measured in triplicate, and after averaging, the base line was subtracted from the sample spectrum. Nucleic acid spectra recorded in either 20 mM HEPES, pH 7.5, 100 mM KCl or in 20 mM sodium phosphate, pH 7.5, 100 mM KF were identical. The phosphate buffer has a much lower absorbance and was used to extend the measurable spectral range from 210 to 180 nm. Thermal melting curves following the ellipticity at 263 (DNA_{1-20}) or 264 nm (hTR_{1-20}) were recorded for each of the quadruplexes in the mentioned HEPES buffer. The spectra were normalized by the number of bases per unit volume. $RHAU_{53-105}$ spectra were identical in 10 mM HEPES, pH 7.5, I = 154 mM (NaCl) or in 10 mM Tris, pH 7.5, I = 154 mM (NaCl). The Tris buffer was used to extend the spectral range to 190 nm because of its more favorable absorption properties. Dialysis into phosphate buffer resulted in a reduced minimum at 200 nm and the substitution of Na^+ with K^+ or of Cl^- with F^- in the formation of aggregates. The spectra were normalized by the number of peptide bonds per unit volume. Protein·nucleic acid complexes were measured in the same HEPES buffer that was used for the nucleic acids, and the spectra were normalized by the number of bases per unit volume (above 250 nm, only the nucleic acid contributes to the spectrum).

Small Angle X-ray Scattering—Scattering data were collected at 20 °C for $RHAU_{53-105}$ (7.0, 8.0, 9.0, and 10.0 mg/ml), $RHAU_{53-150}$ (5.4, 6.4, 7.4, and 8.4 mg/ml), hTR_{1-20} (0.6, 1.0, 1.25, and 1.45 mg/ml), $DNA_{1-20}{}^{C1}$ (0.8, 1.7, 2.2, 3.3, and 4.8 mg/ml), $DNA_{1-20}{}^{C2}$ (3.0, 3.6, and 4.8 mg/ml), $RHAU_{53-105}$·hTR_{1-20} (0.75, 1.0, 1.25, and 1.62 mg/ml), $RHAU_{53-105}$·$DNA_{1-20}{}^{C1}$ (0.75, 1.0, 1.25, and 1.5 mg/ml), and $RHAU_{53-105}$·$DNA_{1-20}{}^{C2}$ (0.9, 1.2, 1.5, and 1.8 mg/ml) in 10 mM HEPES, pH 7.5, I = 154 mM (NaCl) for proteins and 20 mM HEPES, pH 7.5, 100 mM KCl for quadruplexes and protein·nucleic acid complexes (with additional 1 mM EDTA for RNA). Scattering data collection and processing were performed as described previously (34). The radius of gyration (R_g) and maximum particle dimension (D_{max}) were extracted using the GNOM program (35), and solution conformations were determined using DAMMIN (36) with experimental R_g and D_{max} values as constraints for protein, RNA, DNA, and their complexes. The quality of the models was verified by the goodness of fit parameter (χ value) after each model calculation. Individual models for each entity were then rotated and averaged using the program DAMAVER (37). Sample quality was confirmed after SAXS experiments by DLS. The hydrodynamic properties were calculated for each model using the program HYDROPRO (38) to validate models.

Nuclear Magnetic Resonance (NMR) Spectroscopy—NMR samples were prepared in buffers identical to those for SAXS with the exception that a 9:1 H_2O:D_2O mixture was used. All protein spectra were acquired on a Varian Unity INOVA 600-MHz spectrometer, processed with NMRPipe (39), and visualized with Sparky (T. D. Goddard and D. G. Kneller, University of California, San Francisco). To assign the ^1H-^{15}N $RHAU_{53-105}$ HSQC spectrum, ^{15}N,^{13}C-labeled $RHAU_{53-105}$ was subjected to a suite of multidimensional NMR experiments including CBCACONNH, HCCH total correlation spectroscopy, HNCA, HNCACB, HNCACO, HNCO, and NOESY-HSQC. Imino proton spectra were acquired using a Bruker Avance 500-MHz spectrometer and processed/visualized using iNMR.

RESULTS

Solution Conformation of G-quadruplexes—To understand the recognition of quadruplexes by the N-terminal domain of RHAU, an RNA G-quadruplex from human telomerase RNA (comprising nucleotides 1–20 at the 5′-end) was selected as a model system. Purified hTR_{1-20} elutes as a single peak by size exclusion chromatography (Fig. 1*A*), demonstrates monodispersity by DLS (Fig. 1*B*), and stains efficiently with the quadruplex-specific *N*-methyl mesoporphyrin IX dye (Fig. 2*A*). One-dimensional ^1H NMR experiments on purified hTR_{1-20} confirmed that imino protons from guanines and uracils that are protected from solvent exchange due to base pairing cluster to the 10.5–11.5-ppm range (Fig. 2*B*). This is consistent with G-quadruplex formation as opposed to Watson Crick A-U (>13 ppm) or G-C (11.5–13.0 ppm) base pairs. Further evidence of quadruplex formation was obtained using UV-visible spectra of hTR_{1-20} at 20 and 80 °C that revealed significant

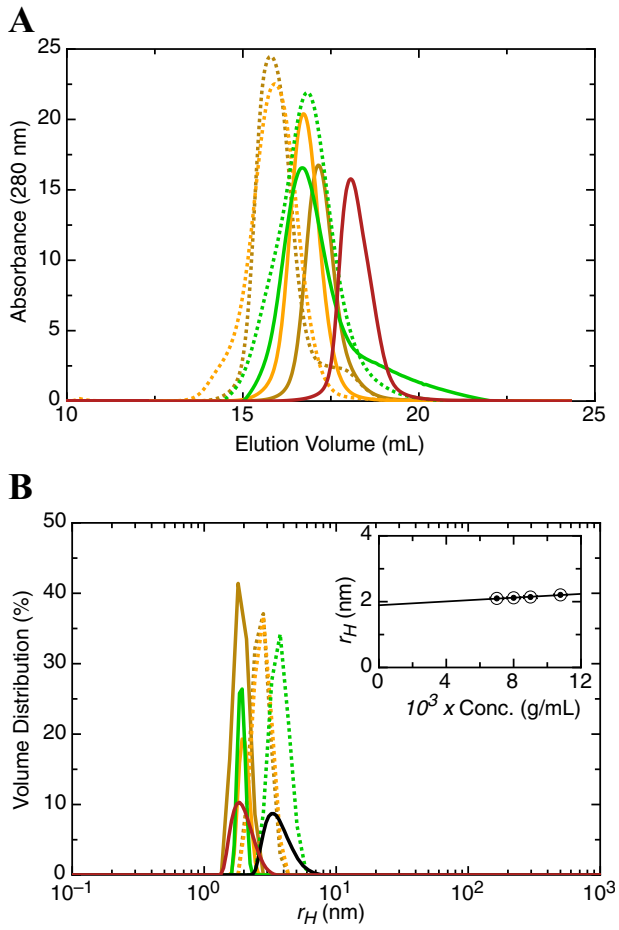

FIGURE 1. **Solution properties of quadruplexes, RHAU N-terminal constructs, and their complexes.** *A*, elution profiles obtained from the Superdex 200 10/300 GL SEC column. *B*, DLS profiles of the studied biomolecules. The concentration (*Conc.*) dependence of the R_h of $RHAU_{53-105}$ is shown in the *inset*. The following color scheme is used: $RHAU_{53-105}$, *red*, *solid*; $RHAU_{53-150}$, *black*, *solid*; hTR_{1-20} RNA, *green*, *solid*; $DNA_{1-20}{}^{C1}$, *orange*, *solid*; $DNA_{1-20}{}^{C2}$, *goldenrod*, *solid*; $RHAU_{53-105}$·hTR_{1-20} RNA, *green*, *dotted*; $RHAU_{53-105}$·$DNA_{1-20}{}^{C1}$, *orange*, *dotted*; $RHAU_{53-105}$·$DNA_{1-20}{}^{C2}$, *goldenrod*, *dotted*.

hypochromicity (20.9%) at 297 nm, a characteristic of the unfolding of a quadruplex structure (25) (Fig. 2*C*).

We next purified the DNA equivalent of hTR_{1-20} (DNA_{1-20}) by SEC to compare it with its RNA counterpart. The procedure separated two distinct DNA conformations, suggesting that although both species have identical molecular weight they may differ slightly in terms of their solution conformation (Fig. 1*A*). To achieve effective separation, a large scale preparatory column was used that resolved two separate peaks: $DNA_{1-20}{}^{C1}$ (first eluted species) and $DNA_{1-20}{}^{C2}$ (second eluted species). Both DNA species migrated similarly and stained efficiently with quadruplex-specific dye (Fig. 2*A*). The imino proton regions of the NMR spectra were again consistent with quadruplex formation for both DNA conformations (Fig. 2*B*). As with the RNA, significant hypochromicity at 297 nm was observed upon heating of both $DNA_{1-20}{}^{C1}$ and $DNA_{1-20}{}^{C2}$, consistent with quadruplex formation (Fig. 2*C*). Comparison of the far-UV CD spectra of hTR_{1-20}, $DNA_{1-20}{}^{C1}$, and $DNA_{1-20}{}^{C2}$ revealed similar overall features, characterized by a maximum ellipticity at 263 (DNA) or 264 nm (RNA) and a minimum at 242 nm. $DNA_{1-20}{}^{C1}$ and $DNA_{1-20}{}^{C2}$ have a second maximum at 207 (C1) or 209 nm (C2), whereas the RNA has a local minimum at this wavelength (Fig. 2*D*). Thermal melting of the quadruplex species resulted in a gradual disappearance of these spectral features (characteristic of quadruplex unstacking) with hTR_{1-20} proving the most resistant to denaturation with a midpoint of the transition above 80 °C followed by $DNA_{1-20}{}^{C1}$ with an estimated midpoint at 70 °C and $DNA_{1-20}{}^{C2}$ at 64 °C (Fig. 2*E*). These values were significantly higher than that expected for single- or double-stranded nucleic acid structures.

The solution conformations of both RNA and DNA quadruplexes were determined by SAXS. As an additional quality control step, we used DLS to ensure monodispersity and suitability for SAXS analysis (Fig. 1*B*). The R_h values determined by DLS for hTR_{1-20}, $DNA_{1-20}{}^{C1}$, and $DNA_{1-20}{}^{C2}$ are similar, and the molecules are monodisperse at high concentration (Fig. 1*B* and Table 1). SAXS data collected at multiple concentrations were merged to obtain a single scattering profile (Fig. 3*A*) that was used to generate the pair distance distribution function ($P(r)$) (a histogram of all observed distances between electron pairs in the molecule), enabling determination of the R_g and the D_{max} for each quadruplex (Fig. 3*B* and Table 1). Based on the scattering data, multiple solution conformations for each quadruplex were generated, rotated, and superimposed to obtain the averaged solution conformation (Fig. 3*C*). Each quadruplex adopts a highly similar disc-shaped structure with a prominent concave bevel at the top and bottom. Near perfect superposition of a high resolution DNA quadruplex structure containing three guanine tetrads (Protein Data Bank code 3SC8 (40)) onto the low resolution models increased our confidence in these low resolution models and orients the guanine tetrad faces with their cavities superimposed on the concave bevels. Model quality was validated through excellent superposition of individually calculated models (normalized spatial discrepancy (NSD) parameter ≤0.51 for each nucleic acid molecule ensemble).

N-terminal Domain of RHAU Mediates an Interaction with hTR—To investigate the interaction between the N-terminal domain of RHAU and hTR quadruplex, we focused on a short truncation of the domain ($RHAU_{53-105}$) that contains the RSM (residues 54–66) and can bind quadruplex *in vitro* (22) (Fig. 4*A*). We have previously demonstrated that endogenous RHAU co-immunoprecipitates with the hTR from HEK293T cell lysates (22). We tested the binding specificity of $RHAU_{53-105}$ by performing RNA interaction assays in HEK293T cell lysates with $RHAU_{53-105}$ purified prior to proteolytic removal of the N-terminal His_6 tag. His_6-tagged $RHAU_{53-105}$ was able to specifically immunoprecipitate (using anti-His_6 antibody) hTR from HEK293T cell lysates in both the presence and absence of endogenous RHAU (Fig. 4*B*). This enrichment was specific to a known RHAU target (hTR) but not to a negative control RNA (GAPDH). Next, we examined the interaction between RHAU and hTR via immunoprecipitations of endogenous RHAU in the presence and absence of an excess of $RHAU_{53-105}$. RNA isolated from RHAU immunoprecipitations demonstrated a ~100-fold enrichment of the telomerase RNA as compared with an equal amount of total RNA. When $RHAU_{53-105}$ was introduced to the cell lysates, this enrichment was reduced ~5-fold, indicating that an excess of $RHAU_{53-105}$ disrupts binding of RHAU to the hTR quadruplex (Fig. 4*C*). Electropho-

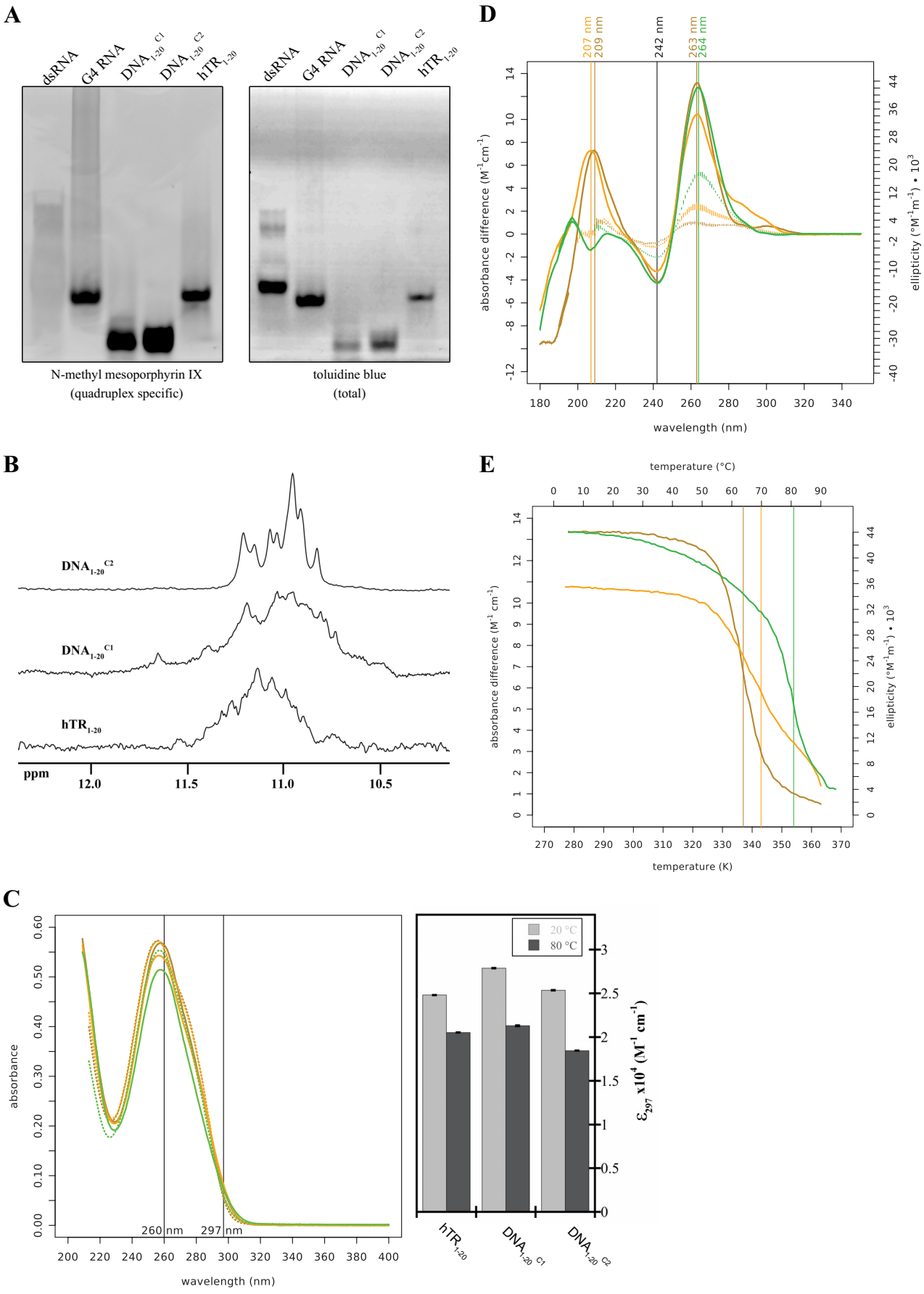
A
dsRNA
G4 RNA
DNA1-20 C1
DNA1-20 C2
hTR1-20
N-methyl mesoporphyrin IX
(quadruplex specific)
toluidine blue
(total)
B
DNA1-20 C2
DNA1-20 C1
hTR1-20
ppm
12.0
11.5
11.0
10.5
C
absorbance
260 nm
297 nm
wavelength (nm)
20 °C
80 °C
ε297 x10^4 (M^-1 cm^-1)
hTR1-20
DNA1-20 C1
DNA1-20 C2
D
207 nm
209 nm
242 nm
263 nm
264 nm
absorbance difference (M^-1cm^-1)
ellipticity (°M^-1m^-1) • 10^3
wavelength (nm)
E
temperature (°C)
absorbance difference (M^-1 cm^-1)
ellipticity (°M^-1m^-1) • 10^3
temperature (K)

TABLE 1
Summary of hydrodynamic data
Errors are indicated in parentheses, and dashes indicate that the values could not be determined.

	$RHAU_{53-105}$		$RHAU_{53-150}$		hTR_{1-20}		$DNA_{1-20}{}^{C1}$	
Hydrodynamic parameter	Experimental	Model-based[d]	Experimental	Model-based[d]	Experimental	Model-based[d]	Experimental	Model-based[d]
r_H(nm)[a]	1.90 (± 0.03)	2.00 (± 0.02)	3.90 (± 0.04)	3.80 (± 0.05)	1.91 (± 0.02)	2.00 (± 0.05)	1.90 (± 0.02)	1.83 (± 0.04)
r_G(nm)[b]	2.1 (± 0.2)	2.2 (± 0.2)	3.25 (± 0.05)	3.37 (± 0.04)	1.31 (± 0.08)	1.40 (± 0.06)	1.34 (± 0.06)	1.48 (± 0.07)
D_{max}(nm)[c]	7.8	8.1 (± 0.1)	12.0	11.90 (± 0.00)	3.4	3.90 (± 0.04)	3.5	3.8 (± 0.04)
r_G/r_H	1.1 (± 0.2)	1.1(± 0.2)	0.83 (± 0.9)	0.88 (± 0.09)	0.7 (± 0.1)	0.7 (± 0.1)	0.71 (± 0.08)	0.81(± 0.08)
χ	-	1.1	-	1.2	-	1.0	-	0.8
NSD	-	0.58 (± 0.06)	-	0.51 (± 0.02)	-	0.48 (± 0.02)	-	0.50 (± 0.01)

	$DNA_{1-20}{}^{C2}$		$RHAU_{53-105}/hTR_{1-20}$		$RHAU_{53-105}/DNA_{1-20}{}^{C1}$		$RHAU_{53-105}/DNA_{1-20}{}^{C2}$	
Hydrodynamic parameter	Experimental	Model-based[d]	Experimental	Model-based[d]	Experimental	Model-based[d]	Experimental	Model-based[d]
r_H(nm)[a]	1.90 (± 0.07)	1.95 (± 0.08)	3.10 (± 0.05)	2.80 (± 0.05)	2.7 (± 0.1)	2.4 (± 0.1)	2.70 (± 0.07)	2.5 (± 0.1)
r_G(nm)[b]	1.41 (± 0.08)	1.57 (± 0.01)	2.60 (± 0.04)	2.70 (± 0.02)	1.78 (± 0.02)	1.9 (± 0.1)	1.82 (± 0.01)	2.0 (± 0.1)
D_{max}(nm)[c]	3.8	4.00 (± 0.04)	8.5	9.2 (± 0.01)	5.0	5.5 (± .05)	5.2	5.60 (± 0.05)
r_G/r_H	0.7 (± 0.1)	0.8 (± 0.1)	0.84 (± 0.09)	0.96 (± 0.07)	0.7 (± 0.1)	0.8(± 0.2)	0.67 (± 0.08)	0.8 (± 0.2)
χ	-	0.9	-	1.1	-	1.2	-	1.1
NSD	-	0.51 (± 0.02)	-	0.52 (± 0.02)	-	0.56 (± 0.02)	-	0.5(± 0.01)

[a] Experimentally determined from DLS data with error obtained from linear regression analysis to infinite dilution from multiple concentrations.
[b] Experimentally determined from SAXS data with error obtained from *P*(*r*) analysis by GNOM.
[c] Experimentally determined from SAXS data obtained from *P*(*r*) analysis by GNOM.
[d] Model-based parameters calculated from HYDROPRO with errors obtained as the S.D. from multiple models.

retic mobility shift assays (EMSAs) at a single protein concentration confirmed that with purified components $RHAU_{53-105}$ shifted hTR_{1-20}, $DNA_{1-20}{}^{C1}$, and $DNA_{1-20}{}^{C2}$ to a similarly sized complex under native conditions (Fig. 4*D*). Dissociation constants for $RHAU_{53-105}$ in complex with hTR_{1-20} (202 ± 17 nM), $DNA_{1-20}{}^{C1}$ (299 + 18 nM), and $DNA_{1-20}{}^{C2}$ (332 ± 24 nM) were estimated based on quantitation of EMSAs at multiple protein concentrations (Fig. 4*E*). Together, these results suggest that $RHAU_{53-105}$ is capable of mediating a specific interaction with hTR.

N-terminal Domain of RHAU Adopts an Extended Conformation—Recombinantly expressed $RHAU_{53-105}$ elutes as a single peak by SEC after affinity tag removal via thrombin digestion (Fig. 1*A*). Sedimentation velocity experiments using analytical ultracentrifugation at multiple concentrations revealed that $RHAU_{53-105}$ remains stable and monomeric with $s^0_{20,w}$ of 0.88 ± 0.05 S (Fig. 5*A*). Interestingly, a frictional ratio (f/f_o) of ~1.40 was obtained from sedimentation velocity data that suggested an extended conformation in solution. DLS analysis at multiple concentrations also confirmed that $RHAU_{53-105}$ is stable and behaves as a monomer (Fig. 1*B*). The far-UV CD spectrum of $RHAU_{53-105}$ shows features of both random coil and ordered secondary structural elements (Fig. 5*B*).

The solution conformation of $RHAU_{53-105}$ was further determined by SAXS using merged data obtained from data collected at multiple concentrations to generate a single scat-

FIGURE 2. **hTR_{1-20} and its DNA analogs adopt a G-quadruplex structure.** *A*, *left*, RNA and DNA G-quadruplexes together with a positive (*G4 RNA*; hTR_{1-43}) and negative (*dsRNA*; HIV-1 trans-activation response element) control were separated by native Tris borate-EDTA polyacrylamide gel electrophoresis and stained with 1 μg/ml *N*-methyl mesoporphyrin IX diluted in 20 mM Tris, pH 7.5, 100 mM KCl, 1 mM EDTA for 15 min at room temperature. *Right*, identical conditions stained for total RNA with toluidine blue. *B*, imino proton regions of hTR_{1-20} (100 μM), $DNA_{1-20}{}^{C1}$ (230 μM), and $DNA_{1-20}{}^{C2}$ (224 μM). *C*, evidence of quadruplex formation was obtained by recording UV-visible spectra at 20 (*solid lines*) and 80 °C (*dotted lines*) for hTR_{1-20} (*green*), $DNA_{1-20}{}^{C1}$ (*orange*), and $DNA_{1-20}{}^{C2}$ (*goldenrod*) that revealed significant hypochromicity for all G-quadruplexes (20.9, 30.9, and 37.5%, respectively) at 297 nm. A modest increase in absorption (hyperchromicity) at 260 nm was also observed over the same transition. At 80 °C, the quadruplexes are only partially unfolded as evidenced in *E*, and the observed differences in hypochromicity between the quadruplexes reflect their distinct thermal stabilities (*inset*). *D*, far-UV CD spectra of hTR_{1-20} (*green*), $DNA_{1-20}{}^{C1}$ (*orange*), $DNA_{1-20}{}^{C2}$ (*goldenrod*) at 20 (*solid line*) and 80 °C (only standard deviations are shown). *Vertical error bars* indicate the standard deviations of three measurements. Maxima and minima of the spectra are indicated by *vertical lines* and the corresponding *wavelength labels*. *E*, melting curves of the G-quadruplexes (*green*, hTR_{1-20}; *orange*, $DNA_{1-20}{}^{C1}$; *goldenrod*, $DNA_{1-20}{}^{C2}$) as monitored by spectropolarimetry at 264 (hTR_{1-20}) and 263 nm (DNA_{1-20}). The estimated midpoints of transitions are indicated by *vertical lines* (hTR_{1-20}, ~81 °C; $DNA_{1-20}{}^{C1}$, 70 °C; $DNA_{1-20}{}^{C2}$, 64 °C).

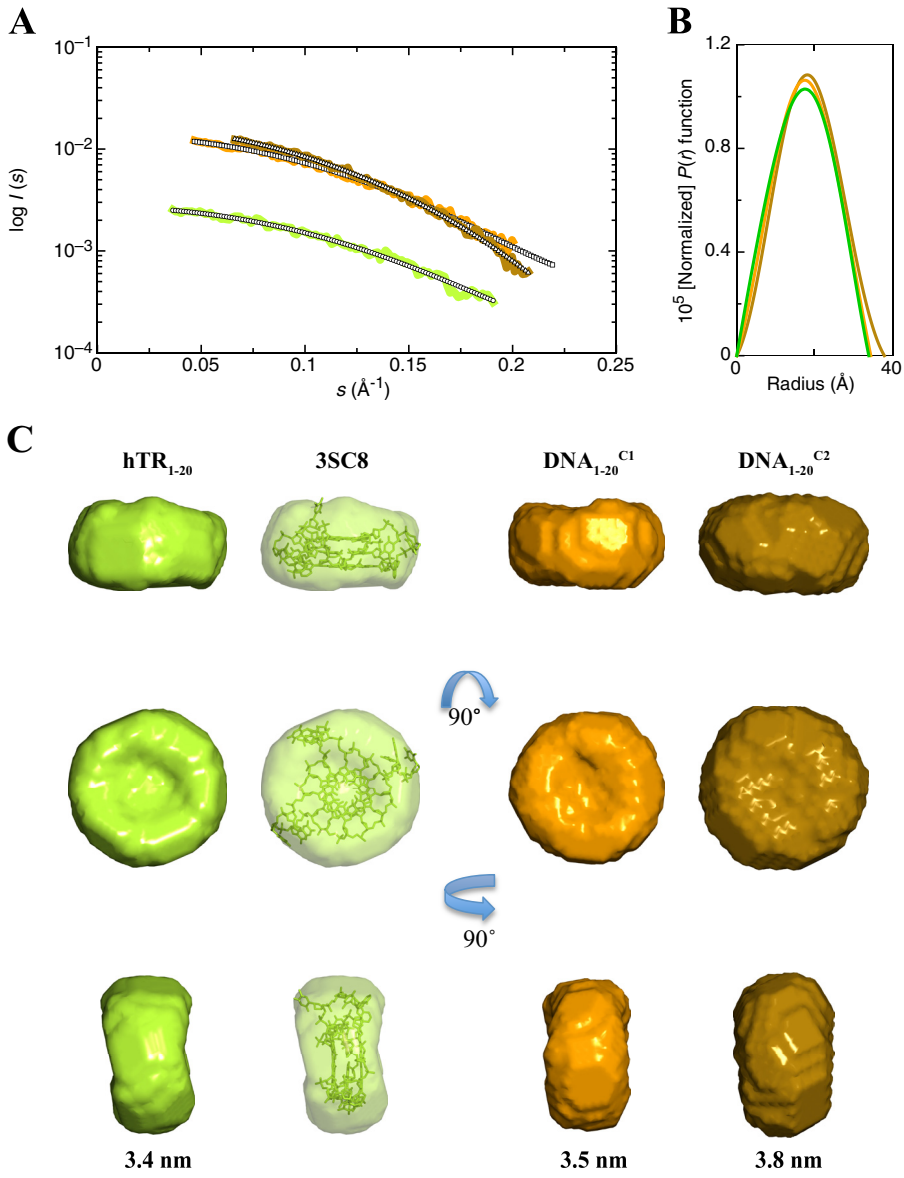

FIGURE 3. **Solution conformation of hTR_{1-20} and its DNA analogs by SAXS.** *A*, merged SAXS data of hTR_{1-20} (*green*), $DNA_{1-20}{}^{C1}$ (*orange*), and $DNA_{1-20}{}^{C2}$ (*goldenrod*) obtained from multiple concentrations for each component. The fit of the calculated scattering profile of the obtained models in *C* to the raw scattering data is superimposed. *B*, corresponding pair distance distribution functions. *C*, low resolution shapes of quadruplexes. The *first column* shows the solution conformation of hTR_{1-20} RNA, and the *second column* shows its superimposition with a high resolution quadruplex structure (Protein Data Bank code 3SC8 (40)). The $DNA_{1-20}{}^{C1}$ and $DNA_{1-20}{}^{C2}$ quadruplexes are presented in *columns 3* and *4*, respectively. The D_{max} is indicated *below* each quadruplex variety.

tering profile (Fig. 5*C*). An extended pair distance distribution function was observed that is typical for an elongated molecule (Fig. 5*D*) with R_g and D_{max} values of 2.1 ± 0.2 and 7.8 nm, respectively (Table 1). Based on the scattering data, multiple solution conformations for $RHAU_{53-105}$ were generated, rotated, and superimposed to obtain an averaged solution conformation (Fig. 5*E*). The NSD parameter of 0.58 ± 0.06 obtained by comparing all models indicates an excellent agreement between independently calculated conformations. Low resolution shape analysis of $RHAU_{53-105}$ revealed an elongated conformation with two well defined subdomains, consistent with an extended and folded structure. Agreement between experimentally determined hydrodynamic parameters and those calculated based solely on the individual SAXS models served to further validate the models (Table 1). Identical DLS results were obtained pre- and post-SAXS data collection, confirming the absence of any radiation damage to the sample after exposure to x-rays. Similarly to $RHAU_{53-105}$, a longer $RHAU_{53-150}$ subdomain also adopts an extended conformation that enabled the assignment of the N- and C-terminal regions of the models (Fig. 5, *C*, *D*, and *E*, and Table 1).

Solution Conformation of N-terminal Domain·Quadruplex Complexes—To determine how the N-terminal domain of RHAU interacts with G-quadruplex, $RHAU_{53-105}$ in complex with hTR_{1-20}, $DNA_{1-20}{}^{C1}$, or $DNA_{1-20}{}^{C2}$ was purified by SEC (Fig. 1*A*). Each complex eluted at a similar volume from the SEC column, formed stoichiometric complexes by EMSAs (Fig. 4*D*), and behaved as a monodisperse species by DLS (Fig. 1*B*). However, a significantly larger R_h was observed for the complex containing hTR_{1-20} (3.10 ± 0.05) *versus* either $DNA_{1-20}{}^{C1}$ (2.7 ± 0.1) or $DNA_{1-20}{}^{C2}$ (2.70 ± 0.07). This difference was further emphasized upon examination of the complexes by

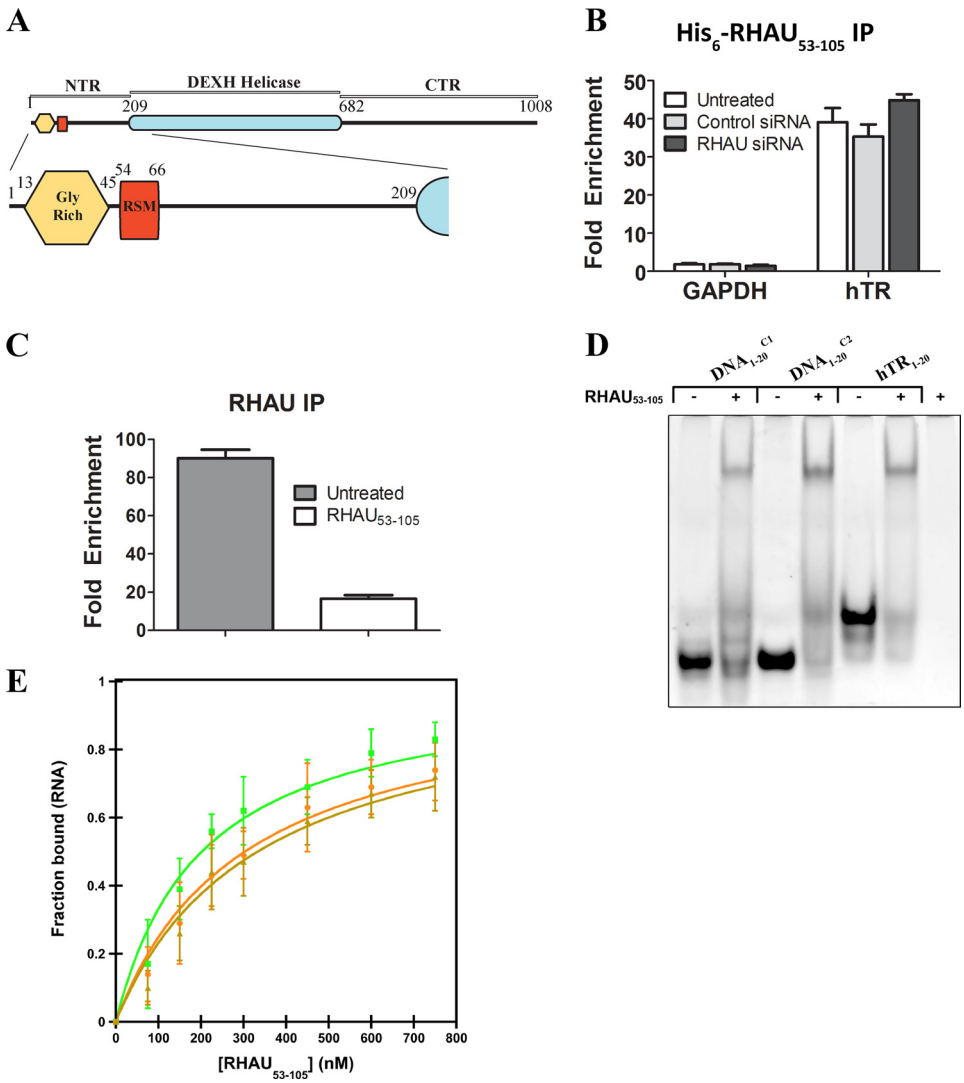

FIGURE 4. **$RHAU_{53–105}$ can form a complex with hTR quadruplex.** *A*, schematic domain representations of RHAU highlighting the RSM located at the N terminus (*NTR*) followed by the DEXH helicase domains and C-terminal region (*CTR*). *B*, HEK293T cells were left untreated or transfected with control or RHAU-specific siRNA for 72 h. Lysates were supplemented with 350 nM His_6-$RHAU_{53–105}$ for 30 min with end-over-end mixing, and RNA·protein complexes were purified using an anti-His_6 antibody. Co-purified RNA was isolated, and both hTR and GAPDH mRNAs were quantified by reverse transcription and PCR. -Fold enrichment was calculated using the comparative C_T method relative to an equal amount of total RNA from each sample. RNAi knockdowns were performed with identical efficiency as shown previously (22). *C*, bar graph representing -fold enrichment of the hTR mRNA as measured by RT-PCR relative to an equal amount of total RNA. RNA co-immunoprecipitated with endogenous RHAU from untreated HEK293T cell lysates and lysates supplemented with 5 μM $RHAU_{53–105}$ was purified and subjected to reverse transcription and PCR using hTR-specific primers. -Fold enrichment was calculated using the comparative C_T method. *D*, EMSAs demonstrate complex formation between $DNA_{1–20}{}^{C1}$, $DNA_{1–20}{}^{C2}$, and $hTR_{1–20}$ with $RHAU_{53–105}$. Nucleic acids were incubated at 200 nM either alone or with 1 μM $RHAU_{53–105}$ for 10 min prior to separation on a 12% native Tris borate-EDTA polyacrylamide gel and stained with SYBR Gold to visualize nucleic acids. *E*, quantitation of EMSA results for $hTR_{1–20}$ (*green*), $DNA_{1–20}{}^{C1}$ (*orange*), and $DNA_{1–20}{}^{C2}$ (*goldenrod*). Nucleic acids were incubated at 150 nM with increasing concentrations of $RHAU_{53–105}$ (0–750 nM) for 10 min prior to separation on a 12% native Tris borate-EDTA polyacrylamide gel and stained with SYBR Gold to visualize/quantify nucleic acids. Experiments were repeated in triplicate with associated S.D. indicated as *error bars*. Dissociation constant determination was performed according to the methodology outlined by Ryder *et al.* (48). *IP*, immunoprecipitation.

SAXS. As described above, scattering data were collected from each complex at multiple concentrations to ensure the absence of self-association and to increase the signal-to-noise ratio (Fig. 6*A*). $RHAU_{53–105}$·$hTR_{1–20}$ presents an extended pair distance distribution function with features that are roughly similar to the free protein but suggests an increased frequency of distances observed in the 4.5–6.5-nm range (Fig. 6*B*). Interestingly, for the RNA complex, the D_{max} increased modestly from 7.8 (free protein) to 8.5 nm (complex), which corresponds approximately to the short edge of the quadruplex disc (Table 1). The average solution conformation based on several models of $RHAU_{53–105}$·$hTR_{1–20}$ shares many of the features of the free protein with the exception of a significant thickening of the N-terminal subdomain upon interaction with quadruplex (Fig. 6*C*). Fitting of the individual average solution conformations of $RHAU_{53–105}$ and $hTR_{1–20}$ into the complex envelope orients the quadruplex at the end of the RSM-containing subdomain and appears to orient the quadruplex such that the guanine tetrad face (largest surface area; contains the concave bevel), and not the sugar-phosphate backbone edges, mediates the interaction with RHAU (Fig. 6*D*). Model and data quality are evidenced by the low NSD (0.52 ± 0.02), indicating excellent superposition of individually calculated models, and a χ

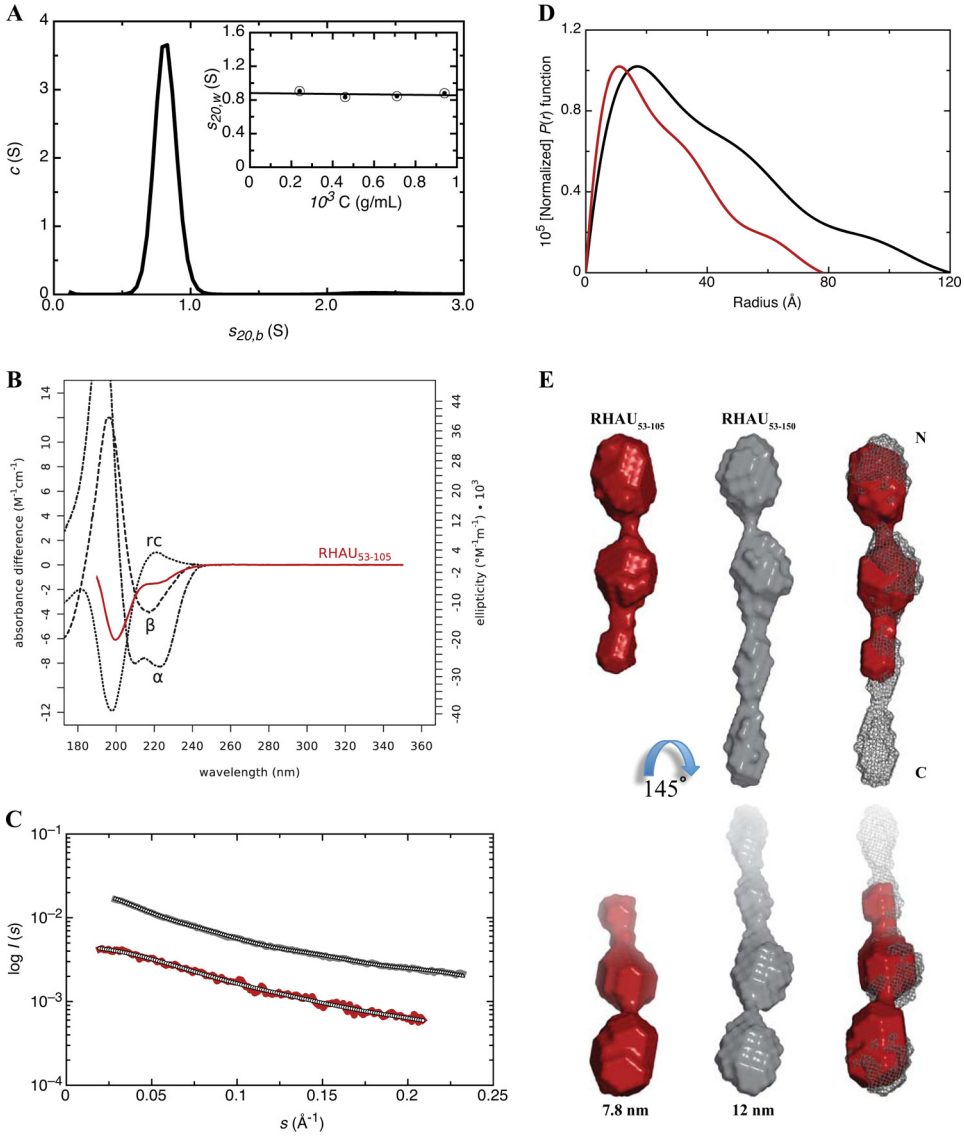

FIGURE 5. **$RHAU_{53–105}$ adopts an extended conformation.** *A*, sedimentation coefficient profile obtained by c(*s*) analysis for $RHAU_{53–105}$ at 0.7 mg/ml indicating its purity. The concentration dependence of the sedimentation coefficient is shown in the *inset*. *B*, far-UV CD spectra of $RHAU_{53–105}$ (*red*) in comparison with reference spectra (49) of secondary structure elements random coil (*rc*), α-helix (α), and β-strand (β). *C*, merged SAXS data for $RHAU_{53–105}$ (*red*) and $RHAU_{53–150}$ (*gray*) obtained from multiple concentrations for each protein. The fit of the calculated scattering profile of the obtained models in *E* to the raw scattering data is overlaid. *D*, corresponding pair distance distribution functions. *E*, averaged low resolution models for $RHAU_{53–105}$ (*left*) and $RHAU_{53–150}$ (*middle*) suggesting an elongated shape of both proteins. Superimposition of the two protein models (*right*) allowed the assignment of the N and C termini. The longitudinal extension (corresponding to D_{max}) is indicated *below* the models.

value of 1.1, indicating good agreement between the individual models calculated and the raw scattering data (Table 1).

Conversely, complexes between $RHAU_{53–105}$ with either DNA quadruplex present a bell-shaped pair distance distribution function and are significantly more compact than the free protein alone or the RNA-containing complex (Fig. 6*B*). Model determination revealed two similar globular average solution conformations for the DNA-containing complexes that lack subdomain definition characteristic of both the free protein and RNA-containing complex (Fig. 6*E*). Rigid body modeling of individual components was therefore not feasible in the context of the DNA complexes.

The RSM Mediates an Interaction with Both RNA and DNA Quadruplex Structures—To attempt to determine the region(s) of the N-terminal domain involved in mediating the interaction, we performed NMR chemical shift perturbation studies on $RHAU_{53–105}$ in the presence and absence of G-quadruplexes. Amide cross-peaks from ^{15}N HSQC spectra of free [^{15}N]$RHAU_{53–105}$ were clustered heavily between 7.5 and 8.5 ppm in the proton dimension, consistent with the extended conformation observed by SAXS and lacking the dispersion characteristic of β-sheet structure (Fig. 7*A*). The spectrum was sufficiently resolved to enable spectral assignments of a large number of amide resonances based on a standard suite of triple resonance experiments. Most importantly, the vast majority of the resonances corresponding to the RSM were unambiguously assigned, including the lone tryptophan side chain amine resonance (Trp-65^{sc}) significantly downfield past 10 ppm in the proton dimension.

To determine the region(s) perturbed in quadruplex binding, we superimposed the HSQC spectra of [^{15}N]$RHAU_{53–105}$, free

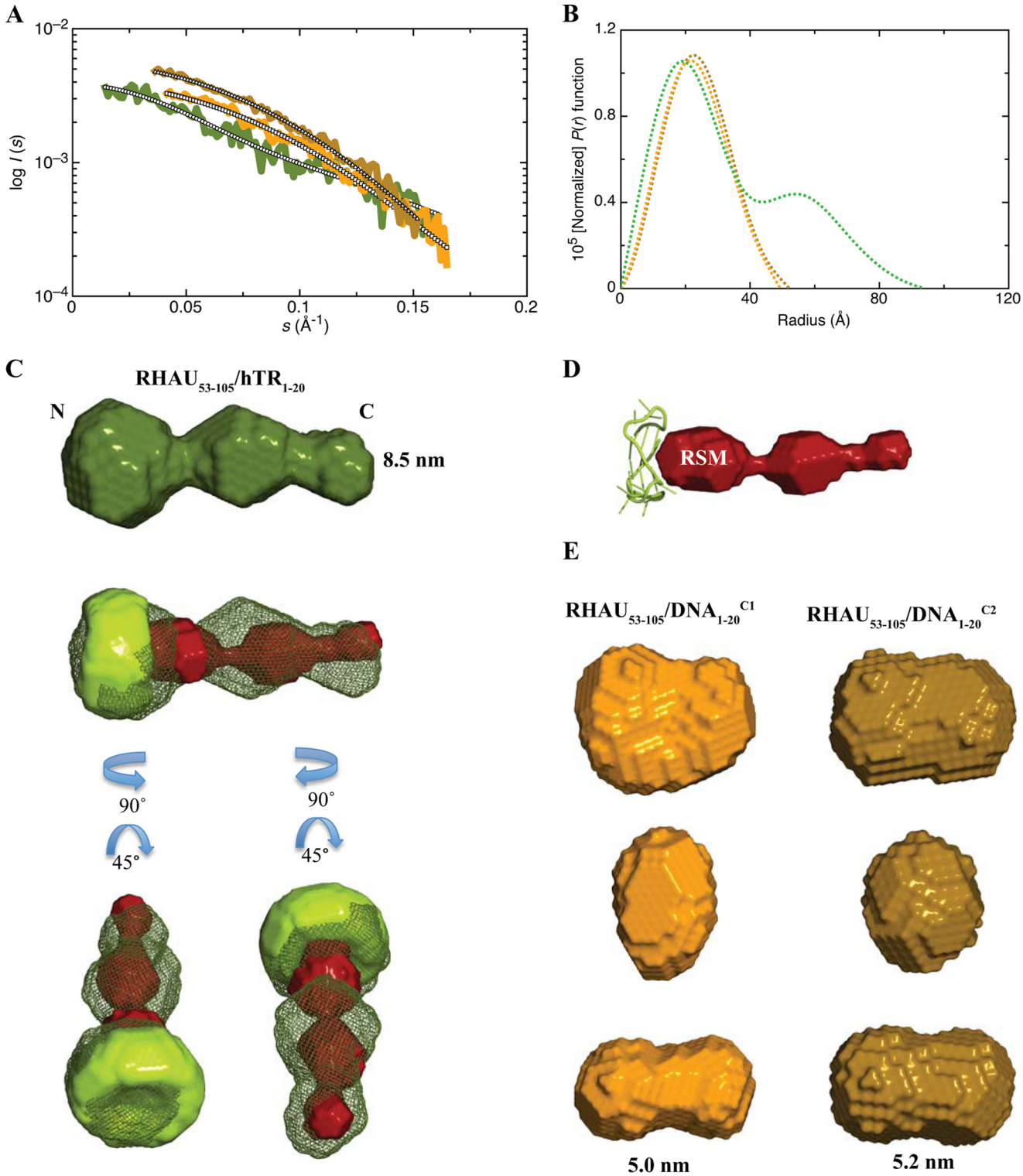

FIGURE 6. **Solution conformations of quadruplex·protein complexes.** *A*, merged SAXS data of $RHAU_{53-105}$·hTR_{1-20} (*green*), $RHAU_{53-105}$·$DNA_{1-20}{}^{C1}$ (*orange*), and $RHAU_{53-105}$·$DNA_{1-20}{}^{C2}$ (*goldenrod*) obtained from multiple concentrations for each complex. The fit of the calculated scattering profile of the determined models in *C* and *E* to the raw scattering data is superimposed. *B*, corresponding pair distance distribution functions. *C*, the *top row* presents the averaged low resolution conformation of $RHAU_{53-105}$·hTR_{1-20} RNA complex that adopts an elongated shape similar to that of $RHAU_{53-105}$. Rigid body superimposition of the individual $RHAU_{53-105}$ and hTR_{1-20} SAXS models onto the complex models suggests that the RSM located at the N terminus of RHAU interacts with hTR_{1-20} RNA (*bottom row*). *D*, proposed scheme of how $RHAU_{53-105}$ interacts with quadruplex (Protein Data Bank code 3SC8 (40)). *E*, the averaged low resolution structures of $RHAU_{53-105}$·$DNA_{1-20}{}^{C1}$ and $RHAU_{53-105}$·$DNA_{1-20}{}^{C2}$ complexes are presented in the *left* and *right columns*, respectively. The D_{max} of each model is indicated *beside* (*C*) and *below* (*E*) the same.

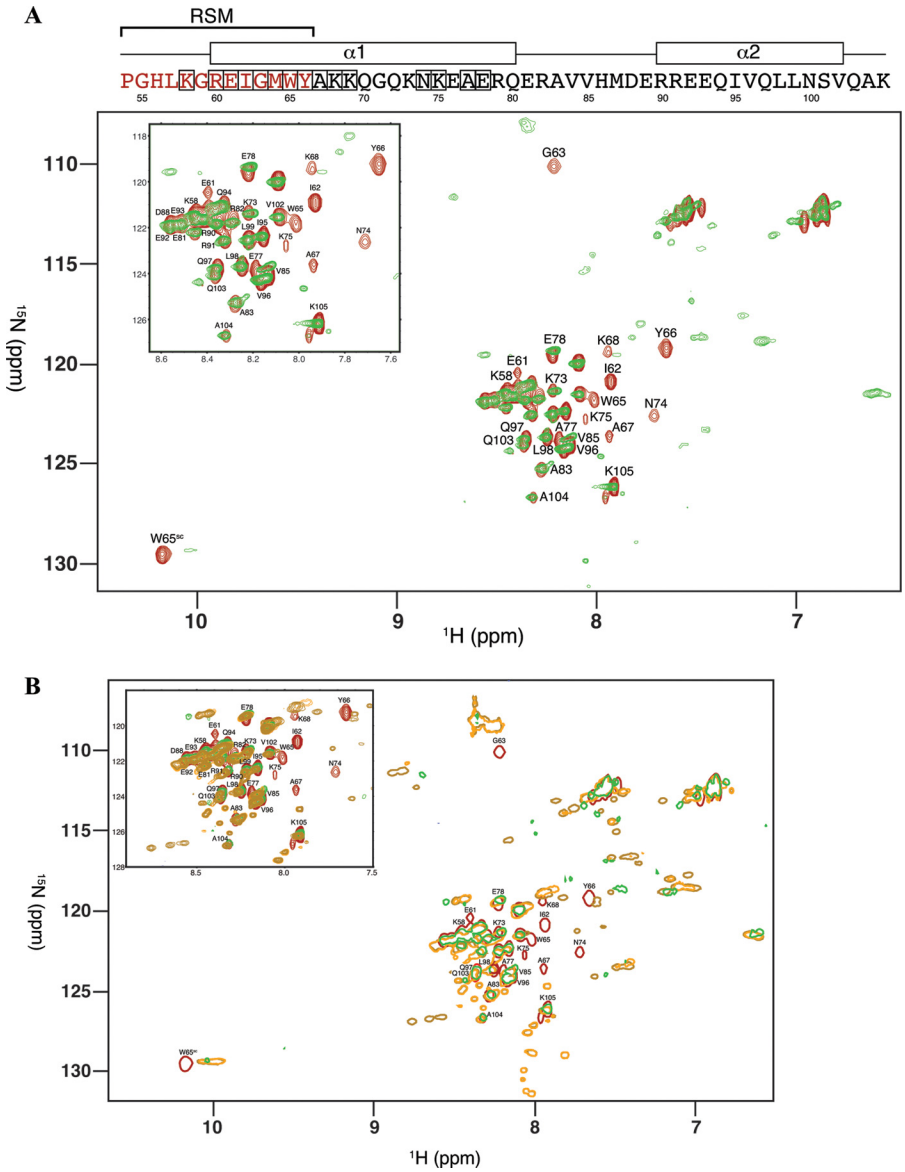

FIGURE 7. **The RSM and α1 helix undergo conformational changes upon quadruplex binding.** *A*, ^{15}N HSQC spectral overlay of $RHAU_{53-105}$, free (*red*) and in complex with hTR_{1-20} (*green*), with a subset of assigned resonances labeled. The predicted secondary structure (26) is shown *above* the spectra together with the primary sequence of $RHAU_{53-105}$. RSM residues in the sequence are colored *red*, and resonances significantly perturbed by hTR_{1-20} binding are *boxed*. Labels for Arg-60, Met-64, and Lys-69 are not shown due to spectral crowding or signal-to-noise issues. *B*, ^{15}N HSQC spectral overlay of $RHAU_{53-105}$, free (*red*) and in complex with hTR_{1-20} (*green*); $DNA_{1-20}{}^{C1}$ (*orange*); or $DNA_{1-20}{}^{C2}$ (*goldenrod*) with a subset of assigned resonances labeled.

and in complex with hTR_{1-20} (Fig. 7*A*). Although the majority of amide resonances were unchanged, significant chemical shift perturbations were observed in the RSM and the adjacent α1 helix (Lys-58, Arg-60, Glu-61, Ile-62, Gly-63, Met-64, Trp-65, Tyr-66, Ala-67, Lys-68, Lys-69, Asn-74, Lys-75, Ala-77, and Glu-78). We repeated NMR experiments using the longer $[^{15}N]RHAU_{53-150}$ to determine the impact of additional C-terminal residues. Although spectral overlap precluded assignment of the amide resonances, comparison of the HSQC spectrum of the protein, free and in complex with hTR_{1-20}, demonstrated that no additional resonances were shifted (data not shown). Notably, a second tryptophan in the longer construct is unperturbed, whereas that in the RSM shifts upon quadruplex binding.

Chemical shift mapping experiments on DNA-containing complexes demonstrated an identical pattern of perturbations in the RSM and adjacent α1 helix as in the complex containing hTR_{1-20} (Fig. 7*B*). Therefore, both RNA and DNA quadruplexes interact in a similar manner with the RSM region of RHAU. In contrast to $[^{15}N]RHAU_{53-105}$·hTR_{1-20}, numerous new resonances appear upon formation of the DNA complexes in various spectral regions. It is an important distinction that these resonances were not originally observable in the spectrum of the free protein, indicating that an unobservable region of the protein has become more ordered upon quadruplex binding. Although we did not attempt assignment of resonances in the DNA complexes, the most straightforward interpretation consistent with the SAXS results is that a second region in addition to the RSM is mediating the interaction with the DNA.

Quadruplex Structure Is Maintained upon Association with N-terminal RHAU—To determine the impact of RHAU binding on perturbation of quadruplex structure, we compared CD

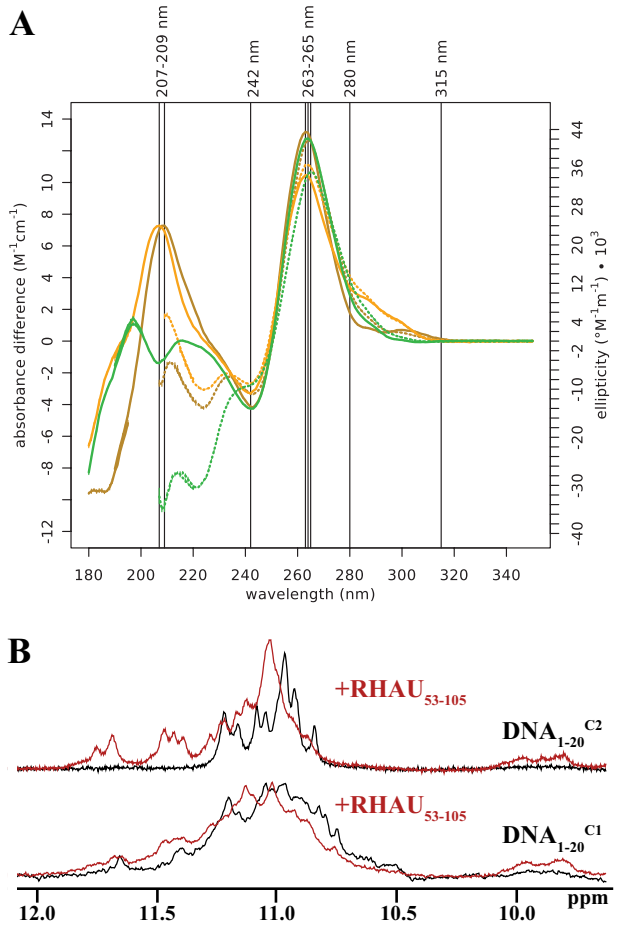

FIGURE 8. **Conformational changes upon protein binding.** *A*, far-UV CD spectra of hTR_{1-20} (*green*), $DNA_{1-20}{}^{C1}$ (*orange*), and $DNA_{1-20}{}^{C2}$ (*goldenrod*). Free G-quadruplexes are indicated by *solid lines*, and those in complex with $RHAU_{53-105}$ are indicated by *dotted lines*. All spectra are on the same scale. All quadruplexes are characterized by a maximum at 263 (DNA) or 264 nm (RNA) that red-shifts by 1 nm upon protein binding and a minimum at 242 nm that does not shift. The DNA quadruplexes have a second maximum at 207 (C1) and 209 nm (C2), respectively, whereas the RNA has a local minimum at this wavelength. Conformational differences between the quadruplexes manifest in the 280–315-nm region. Above 250 nm, only the nucleic acids contribute to the spectra. Below 250 nm, the CD signal is modulated by the protein signal. *B*, NMR chemical shifts of imino protons of $DNA_{1-20}{}^{C1}$ (230 μM) and $DNA_{1-20}{}^{C2}$ (224 μM), either free (*black*) or in equimolar complex with $RHAU_{53-105}$ (*red*).

spectra of the G-quadruplexes in the presence and absence of $RHAU_{53-105}$ (Fig. 8*A*). Binding of $RHAU_{53-105}$ to hTR_{1-20}, $DNA_{1-20}{}^{C1}$, or $DNA_{1-20}{}^{C2}$ does not significantly impact the global shape of the curve above 250 nm (where only the nucleic acid molecule contributes to the spectrum), indicating that the structure of the quadruplex is preserved upon binding of the protein. Conformational differences between the quadruplexes manifest in the 280–315-nm region where the hTR_{1-20} and the $DNA_{1-20}{}^{C1}$ have a sloping shoulder, whereas $DNA_{1-20}{}^{C2}$ has a horizontal shoulder. $DNA_{1-20}{}^{C2}$ undergoes the largest conformational change upon protein binding as indicated by the transformation of the horizontal shoulder into a sloping shoulder similar to that observed in hTR_{1-20}. Examination of the one-dimensional imino proton NMR spectra of $DNA_{1-20}{}^{C1}$ or $DNA_{1-20}{}^{C2}$ alone and in the presence of $RHAU_{53-105}$ confirmed these subtle differences (Fig. 8*B*). Although the quadruplex structure was maintained upon protein binding by both DNA conformations as evidenced by resonances in the 10.5–11.5-ppm range, the imino protons from $DNA_{1-20}{}^{C2}$ are more perturbed downfield upon $RHAU_{53-105}$ binding compared with $DNA_{1-20}{}^{C1}$.

DISCUSSION

RNA and DNA G-quadruplex structures have emerged as important *cis*-acting regulatory elements and have recently been quantitatively visualized in human cells in a number of contexts (11). Although the structural and biophysical characterization of G-quadruplexes has progressed rapidly, the mechanistic basis for their recognition and remodeling is poorly understood. RHAU has emerged as a primary quadruplex resolvase in eukaryotic cells, and the functional consequences of quadruplex remodeling has been established in a small number of important processes (17, 18, 21, 41, 42). Therefore, our goal was to make biophysical inroads to the process by examining the recognition of G-quadruplexes by the N-terminal region of RHAU that contains the RSM, a required region for quadruplex recognition.

Our primary concern with the experimental approach was the biological relevance of using the $RHAU_{53-105}$ truncation to characterize quadruplex recognition. Although the full-length helicase has significantly higher affinity for quadruplex than the N-terminal subdomain (26), we have previously established that $RHAU_{53-105}$ can interact with hTR_{1-20} by EMSA *in vitro* (22) and extended this work to demonstrate that $RHAU_{53-105}$ is capable of mediating an interaction in the context of a cell lysate (Fig. 4). We have demonstrated by a number of biophysical methods that $RHAU_{53-105}$ adopts an extended conformation in which the RSM is likely localized to the largest N-terminal subdomain. It is important to stress that, although extended, the data suggest a well defined, as opposed to a highly dynamic, structure. The solution conformation determined by SAXS in particular reinforces this point as individual models superimpose well on each other (NSD = 0.58 ± 0.06). The observed solution conformation is not unexpected in the context of the full-length protein as it is preceded by a glycine-rich region and followed by a region that we have observed is susceptible to proteolysis (Fig. 4*A*). NMR data on $RHAU_{53-105}$ demonstrate dispersion that is consistent with secondary structure predictions (Fig. 7*A*) and are supported by CD data indicating a mixture of defined secondary structure elements and random coil (Fig. 5*B*).

We present a comprehensive series of SAXS, NMR chemical shift perturbation, CD, DLS, SEC, and analytical ultracentrifugation data to build a strong case for understanding quadruplex recognition by the N-terminal domain of RHAU. SAXS reconstruction suggests that the tetrad face, as opposed to the sugar-phosphate backbone, is the recognition surface for the RSM (Fig. 6*D*). We have deconvoluted the RNA and protein components of the model using rigid body approaches, which are feasible in this situation based on CD and imino proton data indicating minimal perturbation of quadruplex structure (Fig. 8, *A* and *B*). Mutations of charged amino acids in the RSM, which would typically mediate the electrostatic recognition of the sugar-phosphate backbone, have minimal impact on RHAU function (26). Conversely, quadruplex binding and helicase activity are attenuated with small and hydrophobic amino acid mutations in the RSM (26). Qualitatively, the staining intensity of G-quadruplexes bound by $RHAU_{53-105}$ with *N*-methyl

mesoporphyrin IX, a quadruplex-specific dye that stacks on the G-tetrad faces (43), is significantly reduced relative to free quadruplex. This mode of recognition is novel relative to the few existing high resolution structures of a peptide bound to an RNA duplex-quadruplex junction (44) and a telomeric protein·DNA complex (45). NMR chemical shift perturbation experiments indicate that both RNA and DNA quadruplexes perturb identical backbone amide resonances in the RSM and α1 helix of $RHAU_{53-105}$, strongly suggesting that the 2′-OH of the ribose sugar is not required to mediate the interaction (Fig. 7*B*). Although at this point we do not have the resolution to be able to address the importance of different solution conformations observed between the RNA- and DNA-containing complexes, it appears likely that the lack of 2′-OH enables an additional interaction with a region distal to the RSM. Although we await high resolution structures to confirm these observations, the results obtained are consistent with the RSM mediating the recognition but not unwinding of G-quadruplex structure.

Although an increasing number of helicases, including RHAU, have been associated with quadruplex recognition and unwinding, the mechanism of quadruplex unwinding remains elusive. The high resolution structure of Prp43p, an RNA helicase that lacks the N-terminal extension of RHAU but shares significant sequence identity in the core helicase domain and C-terminal extension, revealed homology to existing DNA helicases and the presence of an ATP/Mg^{2+} binding pocket (27, 46). Furthermore, the structure mechanistically suggests that ATP binding/hydrolysis induces a conformational change to expose the RNA binding site required for unwinding/remodeling. We propose a working framework for the recognition of G-quadruplexes by RHAU. The RSM-containing N-terminal region is unique to RHAU and adopts an extended conformation capable of G-quadruplex binding via a G-tetrad face, leaving the sugar-phosphate backbone edges exposed. We do not expect the addition of the glycine-rich region to impede quadruplex binding as a construct retaining an N-terminal His_6 tag and linker does not impede the interaction with hTR in cell lysates (Fig. 4). The specific role of the Gly-rich motif is unclear at this point, although these motifs have been observed proximal to single-stranded RNA recognition motifs to function in RNA binding (47). Connection of the RSM to the core helicase domain via a flexible linker (consistent with our inability to produce a stable RHAU truncation containing residues 151–209) would enable RSM-bound quadruplex to directly access the helicase active site. Alternatively, RSM binding to a quadruplex would enable positioning of the helicase domain on a single-stranded RNA region close by, and translocation through the quadruplex could occur. Whether quadruplex unwinding would ultimately require dissociation from the N-terminal extension of RHAU once the helicase domain is positioned and begins translocation remains an open question. The proposed model is consistent with the observation that RHAU can bind and unwind both DNA and RNA quadruplexes but does not directly provide insight into the substrate specificity of RHAU in terms of either orientation (parallel *versus* antiparallel) or molecularity (uni-, bi-, or tetramolecular) (17). Model confirmation and further mechanistic insights into quadruplex unwinding will await high resolution structure determination of protein comprising both the N-terminal and functional helicase domains.

Acknowledgments—We thank Dr. Michael Freund and the Manitoba Institute for Materials for providing access to SAXS instrumentation and Dr. Joe O'Neil for access to the spectropolarimeter and helpful discussion. We thank Dr. Lynda Donald for assistance with mass spectrometry.

REFERENCES

1. Bochman, M. L., Paeschke, K., and Zakian, V. A. (2012) DNA secondary structures: stability and function of G-quadruplex structures. *Nat. Rev. Genet.* **13,** 770–780
2. Burge, S., Parkinson, G. N., Hazel, P., Todd, A. K., and Neidle, S. (2006) Quadruplex DNA: sequence, topology and structure. *Nucleic Acids Res.* **34,** 5402–5415
3. Marusic, M., Sket, P., Bauer, L., Viglasky, V., and Plavec, J. (2012) Solution-state structure of an intramolecular G-quadruplex with propeller, diagonal and edgewise loops. *Nucleic Acids Res.* **40,** 6946–6956
4. Laughlan, G., Murchie, A. I., Norman, D. G., Moore, M. H., Moody, P. C., Lilley, D. M., and Luisi, B. (1994) The high-resolution crystal structure of a parallel-stranded guanine tetraplex. *Science* **265,** 520–524
5. Wei, D., Parkinson, G. N., Reszka, A. P., and Neidle, S. (2012) Crystal structure of a c-kit promoter quadruplex reveals the structural role of metal ions and water molecules in maintaining loop conformation. *Nucleic Acids Res.* **40,** 4691–4700
6. Wang, Y., and Patel, D. J. (1993) Solution structure of a parallel-stranded G-quadruplex DNA. *J. Mol. Biol.* **234,** 1171–1183
7. Phillips, K., Dauter, Z., Murchie, A. I., Lilley, D. M., and Luisi, B. (1997) The crystal structure of a parallel-stranded guanine tetraplex at 0.95 Å resolution. *J. Mol. Biol.* **273,** 171–182
8. Campbell, N. H., and Neidle, S. (2012) G-quadruplexes and metal ions. *Met. Ions Life Sci.* **10,** 119–134
9. Kaushik, M., Kaushik, S., Bansal, A., Saxena, S., and Kukreti, S. (2011) Structural diversity and specific recognition of four stranded G-quadruplex DNA. *Curr. Mol. Med.* **11,** 744–769
10. Millevoi, S., Moine, H., and Vagner, S. (2012) G-quadruplexes in RNA biology. *Wiley Interdiscip. Rev. RNA* **3,** 495–507
11. Biffi, G., Tannahill, D., McCafferty, J., and Balasubramanian, S. (2013) Quantitative visualization of DNA G-quadruplex structures in human cells. *Nat. Chem.* **5,** 182–186
12. Verma, A., Yadav, V. K., Basundra, R., Kumar, A., and Chowdhury, S. (2009) Evidence of genome-wide G4 DNA-mediated gene expression in human cancer cells. *Nucleic Acids Res.* **37,** 4194–4204
13. Du, Z., Zhao, Y., and Li, N. (2008) Genome-wide analysis reveals regulatory role of G4 DNA in gene transcription. *Genome Res.* **18,** 233–241
14. Huppert, J. L., and Balasubramanian, S. (2007) G-quadruplexes in promoters throughout the human genome. *Nucleic Acids Res.* **35,** 406–413
15. Kumari, S., Bugaut, A., Huppert, J. L., and Balasubramanian, S. (2007) An RNA G-quadruplex in the 5′ UTR of the NRAS proto-oncogene modulates translation. *Nat. Chem. Biol.* **3,** 218–221
16. Siddiqui-Jain, A., Grand, C. L., Bearss, D. J., and Hurley, L. H. (2002) Direct evidence for a G-quadruplex in a promoter region and its targeting with a small molecule to repress c-MYC transcription. *Proc. Natl. Acad. Sci. U.S.A.* **99,** 11593–11598
17. Creacy, S. D., Routh, E. D., Iwamoto, F., Nagamine, Y., Akman, S. A., and Vaughn, J. P. (2008) G4 resolvase 1 binds both DNA and RNA tetramolecular quadruplex with high affinity and is the major source of tetramolecular quadruplex G4-DNA and G4-RNA resolving activity in HeLa cell lysates. *J. Biol. Chem.* **283,** 34626–34634
18. Vaughn, J. P., Creacy, S. D., Routh, E. D., Joyner-Butt, C., Jenkins, G. S., Pauli, S., Nagamine, Y., and Akman, S. A. (2005) The DEXH protein product of the DHX36 gene is the major source of tetramolecular quadruplex G4-DNA resolving activity in HeLa cell lysates. *J. Biol. Chem.* **280,** 38117–38120
19. Pyle, A. M. (2008) Translocation and unwinding mechanisms of RNA and DNA helicases. *Annu. Rev. Biophys.* **37,** 317–336

20. Iwamoto, F., Stadler, M., Chalupníková, K., Oakeley, E., and Nagamine, Y. (2008) Transcription-dependent nucleolar cap localization and possible nuclear function of DExH RNA helicase RHAU. *Exp. Cell Res.* **314,** 1378–1391
21. Huang, W., Smaldino, P. J., Zhang, Q., Miller, L. D., Cao, P., Stadelman, K., Wan, M., Giri, B., Lei, M., Nagamine, Y., Vaughn, J. P., Akman, S. A., and Sui, G. (2012) Yin Yang 1 contains G-quadruplex structures in its promoter and 5′-UTR and its expression is modulated by G4 resolvase 1. *Nucleic Acids Res.* **40,** 1033–1049
22. Booy, E. P., Meier, M., Okun, N., Novakowski, S. K., Xiong, S., Stetefeld, J., and McKenna, S. A. (2012) The RNA helicase RHAU (DHX36) unwinds a G4-quadruplex in human telomerase RNA and promotes the formation of the P1 helix template boundary. *Nucleic Acids Res.* **40,** 4110–4124
23. Lattmann, S., Stadler, M. B., Vaughn, J. P., Akman, S. A., and Nagamine, Y. (2011) The DEAH-box RNA helicase RHAU binds an intramolecular RNA G-quadruplex in TERC and associates with telomerase holoenzyme. *Nucleic Acids Res.* **39,** 9390–9404
24. Sexton, A. N., and Collins, K. (2011) The 5′ guanosine tracts of human telomerase RNA are recognized by the G-quadruplex binding domain of the RNA helicase DHX36 and function to increase RNA accumulation. *Mol. Cell. Biol.* **31,** 736–743
25. Gros, J., Guédin, A., Mergny, J. L., and Lacroix, L. (2008) G-Quadruplex formation interferes with P1 helix formation in the RNA component of telomerase hTERC. *Chembiochem* **9,** 2075–2079
26. Lattmann, S., Giri, B., Vaughn, J. P., Akman, S. A., and Nagamine, Y. (2010) Role of the amino terminal RHAU-specific motif in the recognition and resolution of guanine quadruplex-RNA by the DEAH-box RNA helicase RHAU. *Nucleic Acids Res.* **38,** 6219–6233
27. He, Y., Andersen, G. R., and Nielsen, K. H. (2010) Structural basis for the function of DEAH helicases. *EMBO Rep.* **11,** 180–186
28. Chalupníková, K., Lattmann, S., Selak, N., Iwamoto, F., Fujiki, Y., and Nagamine, Y. (2008) Recruitment of the RNA helicase RHAU to stress granules via a unique RNA-binding domain. *J. Biol. Chem.* **283,** 35186–35198
29. Dzananovic, E., Patel, T. R., Deo, S., McEleney, K., Stetefeld, J., and McKenna, S. A. (2013) Recognition of viral RNA stem-loops by the tandem double-stranded RNA binding domains of PKR. *RNA* **19,** 333–344
30. McKenna, S. A., Lindhout, D. A., Kim, I., Liu, C. W., Gelev, V. M., Wagner, G., and Puglisi, J. D. (2007) Molecular framework for the activation of RNA-dependent protein kinase. *J. Biol. Chem.* **282,** 11474–11486
31. Artimo, P., Jonnalagedda, M., Arnold, K., Baratin, D., Csardi, G., de Castro, E., Duvaud, S., Flegel, V., Fortier, A., Gasteiger, E., Grosdidier, A., Hernandez, C., Ioannidis, V., Kuznetsov, D., Liechti, R., Moretti, S., Mostaguir, K., Redaschi, N., Rossier, G., Xenarios, I., and Stockinger, H. (2012) ExPASy: SIB bioinformatics resource portal. *Nucleic Acids Res.* **40,** W597–W603
32. Patel, T. R., Morris, G. A., de la Torre, J. G., Ortega, A., Mischnick, P., and Harding, S. E. (2008) Molecular flexibility of methylcelluloses of differing degree of substitution by combined sedimentation and viscosity analysis. *Macromol. Biosci.* **8,** 1108–1115
33. Meng, H., Deo, S., Xiong, S., Dzananovic, E., Donald, L. J., van Dijk, C. W., and McKenna, S. A. (2012) Regulation of the interferon-inducible 2′-5′-oligoadenylate synthetases by adenovirus VA(I) RNA. *J. Mol. Biol.* **422,** 635–649
34. Patel, T. R., Morris, G. A., Zwolanek, D., Keene, D. R., Li, J., Harding, S. E., Koch, M., and Stetefeld, J. (2010) Nano-structure of the laminin γ-1 short arm reveals an extended and curved multidomain assembly. *Matrix Biol.* **29,** 565–572
35. Svergun, D. I. (1992) Determination of the regularization parameter in indirect-transform methods using perceptual criteria. *J. Appl. Crystallogr.* **25,** 495–503
36. Svergun, D. I. (1999) Restoring low resolution structure of biological macromolecules from solution scattering using simulated annealing. *Biophys. J.* **76,** 2879–2886
37. Volkov, V. V., and Svergun, D. I. (2003) Uniqueness of *ab initio* shape determination in small-angle scattering. *J. Appl. Crystallogr.* **36,** 860–864
38. García De La Torre, J., Huertas, M. L., and Carrasco, B. (2000) Calculation of hydrodynamic properties of globular proteins from their atomic-level structure. *Biophys. J.* **78,** 719–730
39. Delaglio, F., Grzesiek, S., Vuister, G. W., Zhu, G., Pfeifer, J., and Bax, A. (1995) NMRPipe: a multidimensional spectral processing system based on UNIX pipes. *J. Biomol. NMR* **6,** 277–293
40. Collie, G. W., Promontorio, R., Hampel, S. M., Micco, M., Neidle, S., and Parkinson, G. N. (2012) Structural basis for telomeric G-quadruplex targeting by naphthalene diimide ligands. *J. Am. Chem. Soc.* **134,** 2723–2731
41. Tran, H., Schilling, M., Wirbelauer, C., Hess, D., and Nagamine, Y. (2004) Facilitation of mRNA deadenylation and decay by the exosome-bound, DExH protein RHAU. *Mol. Cell* **13,** 101–111
42. Kim, H. N., Lee, J. H., Bae, S. C., Ryoo, H. M., Kim, H. H., Ha, H., and Lee, Z. H. (2011) Histone deacetylase inhibitor MS-275 stimulates bone formation in part by enhancing Dhx36-mediated TNAP transcription. *J. Bone Miner. Res.* **26,** 2161–2173
43. Nicoludis, J. M., Miller, S. T., Jeffrey, P. D., Barrett, S. P., Rablen, P. R., Lawton, T. J., and Yatsunyk, L. A. (2012) Optimized end-stacking provides specificity of N-methyl mesoporphyrin IX for human telomeric G-quadruplex DNA. *J. Am. Chem. Soc.* **134,** 20446–20456
44. Phan, A. T., Kuryavyi, V., Darnell, J. C., Serganov, A., Majumdar, A., Ilin, S., Raslin, T., Polonskaia, A., Chen, C., Clain, D., Darnell, R. B., and Patel, D. J. (2011) Structure-function studies of FMRP RGG peptide recognition of an RNA duplex-quadruplex junction. *Nat. Struct. Mol. Biol.* **18,** 796–804
45. Horvath, M. P., and Schultz, S. C. (2001) DNA G-quartets in a 1.86 Å resolution structure of an *Oxytricha nova* telomeric protein-DNA complex. *J. Mol. Biol.* **310,** 367–377
46. Walbott, H., Mouffok, S., Capeyrou, R., Lebaron, S., Humbert, O., van Tilbeurgh, H., Henry, Y., and Leulliot, N. (2010) Prp43p contains a processive helicase structural architecture with a specific regulatory domain. *EMBO J.* **29,** 2194–2204
47. Mangeon, A., Junqueira, R. M., and Sachetto-Martins, G. (2010) Functional diversity of the plant glycine-rich proteins superfamily. *Plant Signal. Behav.* **5,** 99–104
48. Ryder, S. P., Recht, M. I., and Williamson, J. R. (2008) Quantitative analysis of protein-RNA interactions by gel mobility shift. *Methods Mol. Biol.* **488,** 99–115
49. Brahms, S., and Brahms, J. (1980) Determination of protein secondary structure in solution by vacuum ultraviolet circular dichroism. *J. Mol. Biol.* **138,** 149–178